

# SCIENTIFIC REPORTS



OPEN

## Magnetic domain walls as broadband spin wave and elastic magnetisation wave emitters

Rasmus B. Holländer<sup>1</sup>, Cai Müller<sup>1</sup>, Julius Schmalz<sup>2</sup>, Martina Gerken<sup>1</sup> <sup>2</sup> & Jeffrey McCord<sup>1</sup>

We report on the direct observation of spin wave and elastic wave emission from magnetic domain walls in ferromagnetic thin films. Driven by alternating homogeneous magnetic fields the magnetic domain walls act as coherent magnetisation wave sources. Directional and low damped elastic waves below and above the ferromagnetic resonance are excited. The wave vector of the magnetoelastically induced acoustic waves is tuned by varying the excitation frequency. The occurrence of elastic wave emission is proved by a combination of micromagnetic and mechanical finite element simulations. Domain wall emitted magnetostatic surface spin waves occur at higher frequencies, which characteristics are confirmed by micromagnetic simulations. The distinct modes of magnetisation wave excitation from micromagnetic objects are a general physical phenomenon relevant for dynamic magnetisation processes in structured magnetic films. Magnetic domain walls can act as reconfigurable antennas for spin wave and elastic wave generation. The wave orientation can be controlled separately via the domain wall orientation for elastic waves and via magnetization orientation for magnetostatic surface spin waves.

Relying on local excitation, spin waves offer the possibility to substitute modern day electronics by wave-computing<sup>1–3</sup>. Different kinds of applications like spin wave logic devices, signal processors, and devices involving spin wave mediated spin currents are projected. Spin wave excitation in magnetic films is generally based on small lateral antennas for the local excitation of spin waves. One approach towards application oriented spin wave technology focusses on the interaction between spin waves and naturally occurring magnetic microstructures at edges<sup>4,5</sup> and magnetic domain walls<sup>6</sup>. In that context, symmetric Bloch type domain walls and their spin wave eigenmodes have long been studied<sup>7</sup>. Theoretical predictions include numeric and analytical models in uniaxial<sup>8</sup> and cubic ferromagnetic materials<sup>9</sup>. Beyond regular Bloch walls, in patterned magnetic thin films different types of magnetic domain walls form. Dynamic spin wave experiments involving magnetic textures range from Néel domain walls for mode localization and guidance of spin wave modes<sup>10,11</sup> to magnetic domain walls as a delimiter for spin waves<sup>12</sup> to excited magnetic vortex cores<sup>13</sup>. Numerical studies suggest the utilisation of domain walls as directional spin wave emitters<sup>14,15</sup>. An evidence of such a behaviour was shown only once<sup>16</sup>. In general, for magnetic thin films dynamic domain wall effects maximize at excitation frequencies around the specific domain wall resonance, which fundamentally is below the ferromagnetic resonance of the magnetic host material<sup>17–19</sup>.

The possible generation of elastic magnetisation waves from local elastic strains was investigated numerically<sup>20</sup> by solving the Landau-Lifshitz-Gilbert equation together with the elastodynamic equations using finite element simulations. A piezoelectric element generates local dynamic strain which is transferred to a magnetostrictive material. The simulations predict low loss characteristics for the elastic waves leading to enhanced magnetisation wave propagation lengths as compared to conventional field generated spin waves. The elastic magnetisation wave<sup>21</sup> excitation from local piezoelectric antennas due to excitation of alternating strain induced anisotropy in magnetostrictive ferromagnetic layers was shown experimentally<sup>22</sup>. Alternatively, it was suggested that magnetic domain walls in magnetostrictive materials may also radiate elastic waves from domain walls through magnetoelastic coupling of a moving or vibrating domain wall<sup>23</sup>. Changes of magnetisation inside the domain wall are directly transferred to local modulation of strain through magnetostriction. Yet, the theoretical study was limited to the MHz-regime. No direct experimental proof for the described modes of wave radiation are reported so far.

<sup>1</sup>Institute of Materials Science, Kiel University, Kiel, 24143, Germany. <sup>2</sup>Institute of Electrical and Information Engineering, Kiel University, Kiel, 24143, Germany. Correspondence and requests for materials should be addressed to R.B.H. (email: [rh@tf.uni-kiel.de](mailto:rh@tf.uni-kiel.de)) or J.M. (email: [jmc@tf.uni-kiel.de](mailto:jmc@tf.uni-kiel.de))

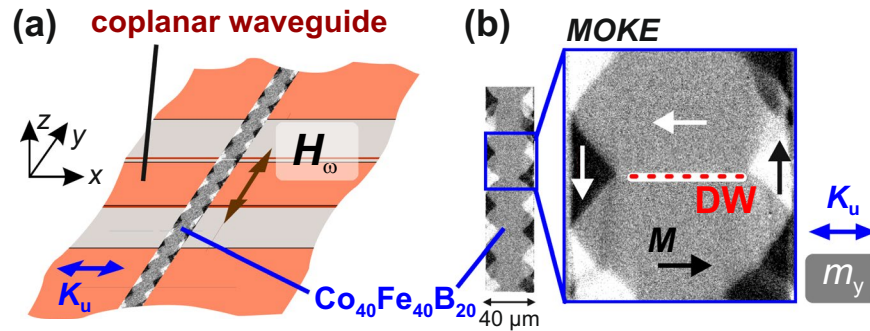


**Figure 1.** Excitation scheme and experimental evidence. (a) Amorphous  $\text{Co}_{40}\text{Fe}_{40}\text{B}_{20}$  stripe with the easy axis of magnetisation  $K_u$  perpendicular to the long axis of the stripe excited by the homogeneous Oersted field on top of a coplanar waveguide with a  $160\ \mu\text{m}$  wide and  $17.5\ \mu\text{m}$  thick centre conductor. The sample is flipped upside-down with the magnetic structure facing the wave guide. (b) Static ferromagnetic domain configuration after application of a saturating bias field along the  $x$ -axis, exhibiting a wide domain state (WDS). The position of the high angle domain wall (DW) is indicated.

The inverse magnetoelastic behaviour, the coupling from elastic waves to magnetisation dynamics has also been investigated. It was shown that elastic waves can interact with magnetic textures, such as magnetic vortices<sup>24</sup>. In<sup>25</sup> it was shown that elastic waves induce precessional motion of magnetisation in a magnetostrictive thin film deposited on a piezoelectric substrate through strain mediation.

Here, we focus on the excitation of spin waves and elastic magnetisation waves from magnetic domain walls. Domain walls with nanometer core width offer the opportunity for local and reconfigurable spin wave devices, by flexible positioning of the domain walls. We prove the antenna free emission of magnetostatic spin waves and, in particular, elastic magnetisation waves in ferromagnetic films from asymmetric Bloch and Néel type domain walls<sup>26</sup> by direct time-resolved magneto-optical imaging in conjunction with complementary simulations. We show that domain walls offer an alternative and flexible excitation scheme for elastic magnetisation waves and spin waves.

## Results

**Experimental evidence of magnetisation wave emission.** The investigated model system consists of a magnetostrictive amorphous ferromagnetic  $\text{Co}_{40}\text{Fe}_{40}\text{B}_{20}$  film with a thickness of  $d_{\text{CoFeB}} = 120\ \text{nm}$  deposited on a transparent glass substrate. To ensure the reproducible generation of domain walls the film is patterned into elongated stripes. Asymmetric  $180^\circ$  Bloch walls form for this ferromagnetic layer thickness<sup>26</sup>. With the application of a magnetic bias field aligned perpendicular to the domain wall, the domain wall angle is reduced and asymmetric Néel walls form. For the standard experiment (Fig. 1(a)), the axis of uniaxial anisotropy  $K_u$  is aligned perpendicular to the stripe axis along the  $x$ -direction. In Fig. 1(b) a typical static remanent magnetisation state imaged by magneto-optical Kerr effect (MOKE) microscopy<sup>27</sup> is shown, displaying a wide domain state (WDS). In the centre of the magnetic stripe, a periodic pattern of domains aligned parallel and antiparallel to the  $x$ -direction is obtained in the remanent state after applying a magnetic field along  $x$ .

Dynamic magnetisation component-selective MOKE response<sup>28</sup> images are displayed in Fig. 2. The differential time evolution of the individual magnetisation components  $\Delta m_x$ ,  $\Delta m_y$ , and  $\Delta m_z$  are shown for three different times  $t$ . The excitation frequency of the sinusoidal varying field  $H_{\omega,y}$  was set to the domain resonance  $\omega_{\text{res}}/2\pi = 1.9\ \text{GHz}$ . While  $\Delta m_y$  and  $\Delta m_z$  indicate a strong uniform precession of the domains around the easy axis of magnetisation,  $\Delta m_x$  shows only small deviations in time. The main features at the boundary to the closure domains visible in  $\Delta m_x$  correspond to the nature of a magnetically charged domain state at the edges. In  $\Delta m_y$  and  $\Delta m_z$  small periodic features appear inside the excited domains parallel to the domain wall. In the following, we focus on the magnetisation waves emitted by the central domain walls. As we show, these correspond to coherent elastic wave superpositions resulting from wave emission from the dynamically excited domain walls.

**Domain wall dependent emission.** To prove the direct connection of the elastic wave generation to the magnetic domain walls we investigated the dependence of wave excitation on the domain and domain wall configuration. To ensure comparability each domain state was measured at its ferromagnetic resonance. Figure 3(a) shows the wave generation in a canted domain state (CDS). The CDS was created from the zero field WDS state by applying a bias field  $H_y = 640\ \text{A/m}$  along the  $y$ -direction. The magnetisation in the centre domains is tilted by  $10^\circ$  relative to  $K_u$  as indicated in Fig. 3(a). Here, the domain walls transform from asymmetric Bloch to asymmetric Néel wall<sup>26</sup>, confirmed by MOKE imaging with the sensitivity aligned perpendicular to the domain wall (not shown). The time evolution of the out-of-plane MOKE contrast  $c \cdot \Delta m_z$  displays wavefronts aligned parallel to the domain wall at the same excitation frequency of  $\omega/2\pi = 1.9\ \text{GHz}$  as used for the experiments shown in Fig. 2. With the altered domain wall characteristics, the orientation and characteristics of the elastic waves remain. The wave vector does not follow the rotation of magnetisation.

By changing the domain width and field excitation frequency the elastic waves remain excited. Figure 3(b) shows a narrow domain state (NDS) generated by saturating the stripe along the  $y$ -direction and reducing the

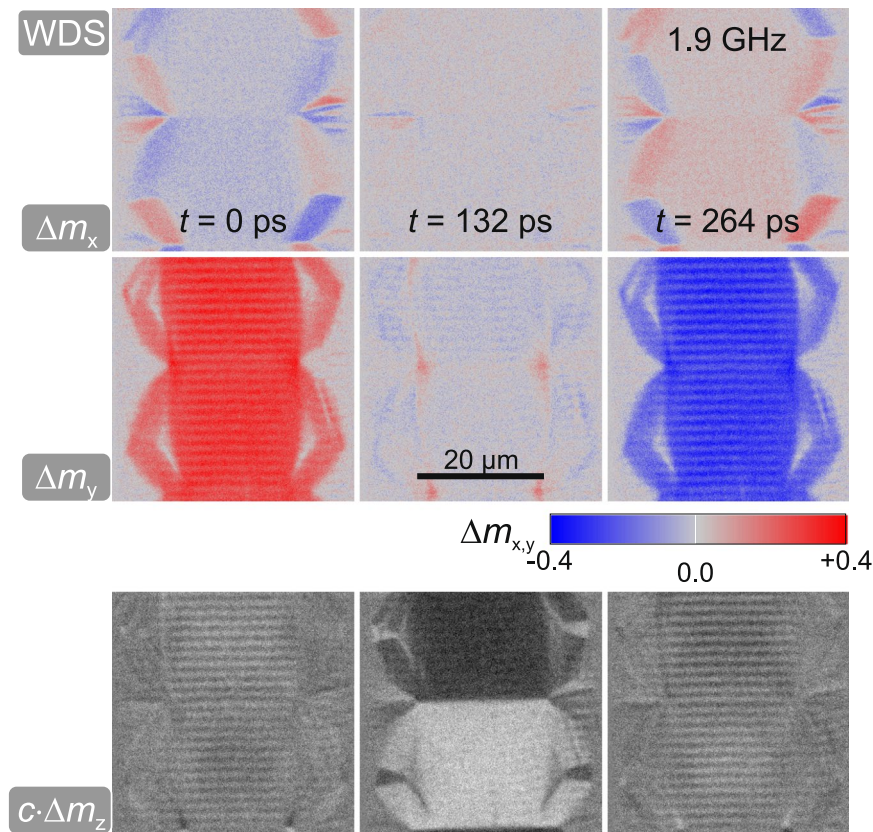


**Figure 2.** Differential dynamic magnetisation response images along three different magneto-optical sensitivity directions at  $t = 0$  ps,  $t = 132$  ps, and  $t = 264$  ps driven at the domain precessional frequency at 1.9 GHz with an amplitude of  $H_{\omega,y} \approx 150$  A/m.

external field  $H_y$  to zero. The narrow domain width leads to different effective fields as compared to Fig. 1(b), giving rise to a higher domain resonance frequency<sup>29,30</sup> of  $\omega_{res}/2\pi = 2.5$  GHz. From the time evolution of  $\Delta m_y$ , it is directly apparent that the periodicity of the elastic waves shifted to smaller wavelengths. The static NDS shows various domain widths, leading to locally varying effective fields. The wavelength of the elastic wave is unaffected by the local effective fields.

A dependency on geometric factors like stripe orientation is excluded by changing the orientation of the domain walls relative to the excitation field and stripe axis. Figure 3(c) depicts a WDS with slightly tilted anisotropy. Statically the  $m_x$  component is shown, while the time evolution was recorded with oblique plane of incidence resulting in a superposition of longitudinal and polar magneto-optical contrast ( $\Delta m_y + c \cdot \Delta m_z$ ). Due to the alignment of the anisotropy the domain wall is oriented with an angle of  $4.5^\circ$  to the  $x$ -axis. It is directly evident that the wave pattern follows the domain wall orientation and not the orientation of the magnetic track. In order to exclude the possibility of purely microwave field generated waves, an additional control experiment was performed, where the magnetic sample was turned with reference to the excitation source. Figure 3(d) displays these results for a WDS. Here, the static image displays the  $m_y$  component of magnetisation and the time evolution of magnetisation changes shows a superposition of longitudinal and polar contrast ( $\Delta m_y + c \cdot \Delta m_z$ ). The axis of oscillating magnetic field resided along the  $y$ -axis, while the long axis of the magnetic stripe was oriented  $17^\circ$  compared to the  $y$ -axis.

Finally, no magnetization waves form in the absence of magnetic domain walls. An additional configuration without high-angle domain walls is depicted in Fig. 3(e), where a bias field of  $H_x = 3$  kA/m was applied along the  $x$ -direction to obtain a nearly saturated domain state. In contrast to the examples before and in the absence of magnetic domain walls no elastic waves are excited. The experiments prove that the wave source is not the microwave field. The elastic wave generation and orientation is directly bound to the existence and orientation of the magnetic domain walls and independent of the alignment of magnetisation.

The ability to tune the emission of domain wall bound waves is demonstrated by measuring the elastic magnetisation wave characteristics in an identical WDS configuration with the excitation frequency ranging from  $\omega/2\pi = 0.7$  GHz to  $\omega/2\pi = 2.5$  GHz. Exemplary results extracted from the centre domain at three different excitation frequencies are displayed in Fig. 4. To clearly exhibit the wave character at these selected frequencies, the precession of the domain was removed by subtracting the spatial average over an individual time frame, i.e.  $\Delta m_y - \langle \Delta m_y \rangle_{x,y}$  is depicted. The change in wavelength of the elastic magnetisation waves, and thus, the dispersion relation of the excited coherent elastic waves are directly imaged. From the images it is evident that the wavelength of the superimposed elastic waves decreases with increasing excitation frequency. We interpret

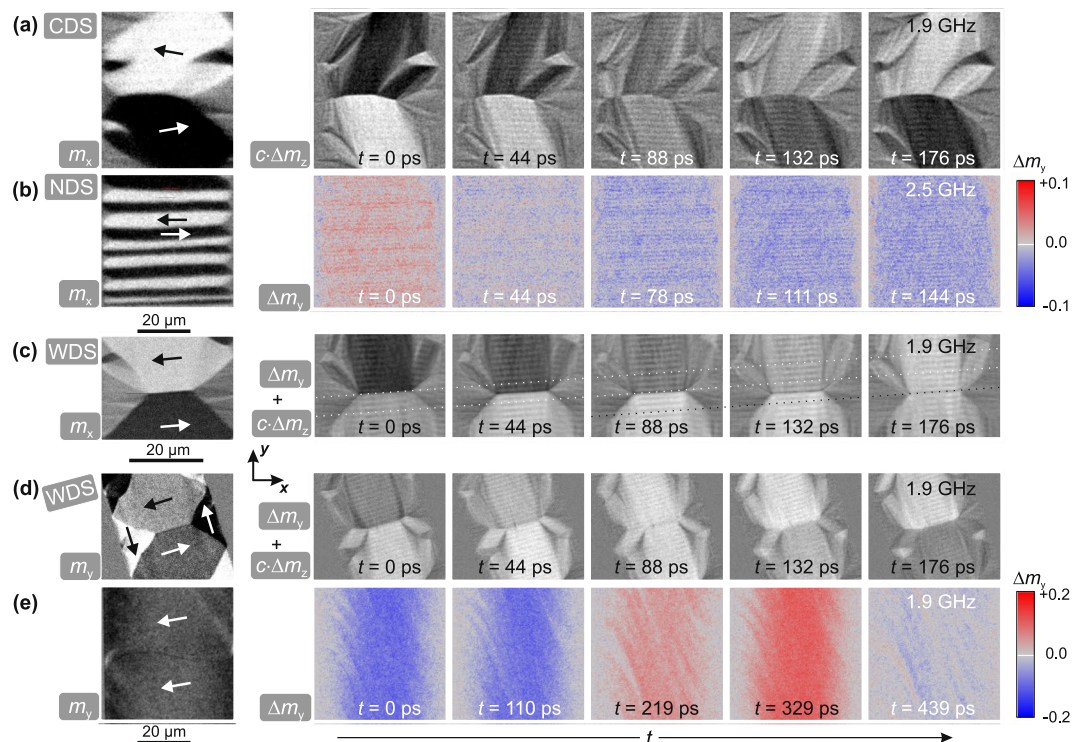


**Figure 3.** (a) Static domain configuration and time evolution of a canted domain state (CDS) by application of a small bias field along the  $y$ -direction to a wide domain state (WDS). The static magnetisation component along the  $x$ -axis and the out-of-plane time evolution are shown. (b) A narrow domain state (NDS) at zero field created by field history perpendicular to uniaxial anisotropy. The static  $x$ -component of magnetisation is shown, while the time evolution shows pure longitudinal contrast along the  $y$ -direction. (c) Static and dynamic behaviour with tilted orientation of magnetisation and domain wall orientation in the WDS state and (d) with tilted sample orientation. Static and dynamic images are obtained with oblique plane of incidence. (e) Magnetic domain state close to saturation by applying a bias field parallel to the  $x$ -axis. The static component along the  $y$ -direction is depicted as well as the pure longitudinal time evolution along the  $y$ -direction.  $H_{\omega,y} = 150$  A/m was applied for all dynamic images. Principal directions of magnetisation are indicated in the static images.

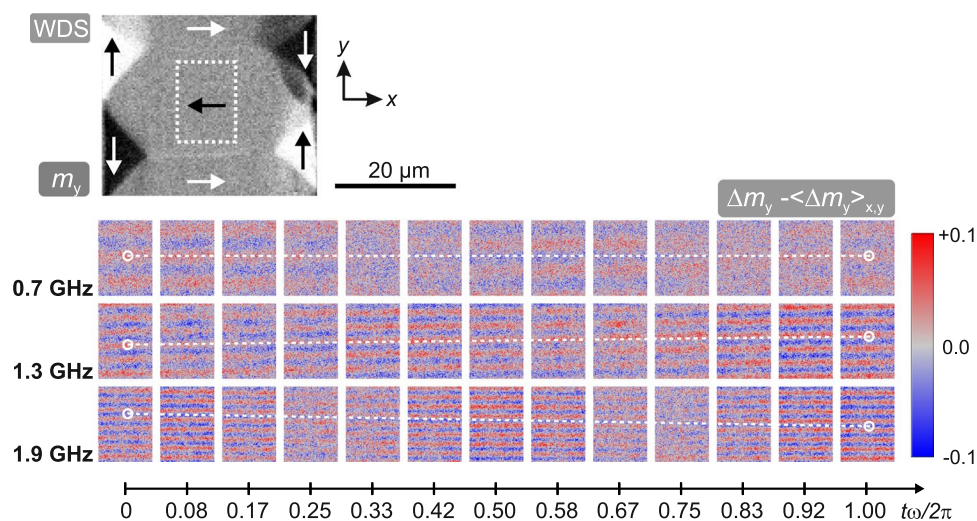


**Figure 4.** Time evolution of an individual domain in the same WDS with the magneto-optical sensitivity along the  $y$ -direction at different excitation frequencies of  $\omega/2\pi = 0.7$  GHz,  $\omega/2\pi = 1.3$  GHz, and  $\omega/2\pi = 1.9$  GHz (see also Supplementary Video 1). The analysed domain region is indicated in the static domain image. An Oersted field amplitude of  $H_{\omega} = 295$  A/m was used for the experiments. Lines for eye-guidance are drawn to show the wave propagation.

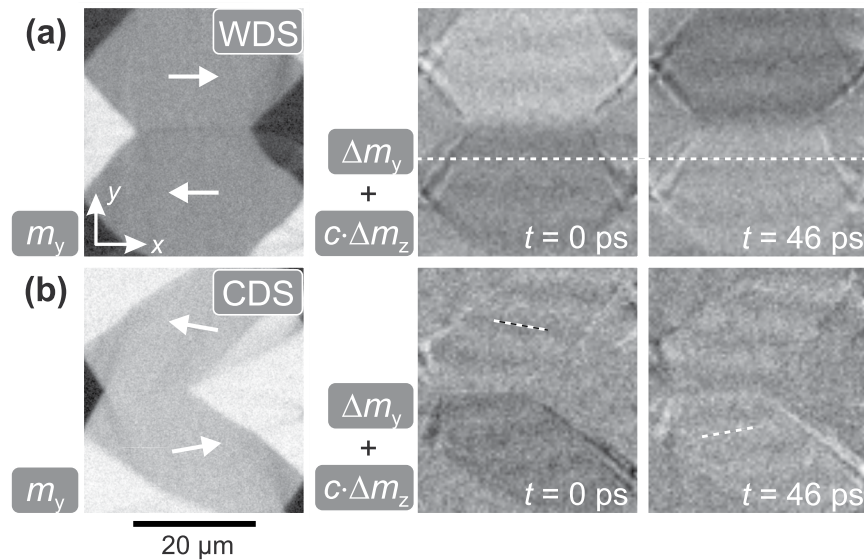


**Figure 5.** Static configuration and time evolution of magnetisation at  $\omega/2\pi = 9$  GHz excitation for (a) a remanent domain configuration (WDS) with field history along the axis of uniaxial anisotropy (see also Supplementary Video 2 for  $c \cdot \Delta m_z$ ) and (b) a canted domain state (CDS) by application of a small bias field along the  $y$ -direction. Principal directions of magnetisation are indicated. The time evolution shows the qualitative magneto-optical magnetisation response as superposition of longitudinal and polar contrast. An excitation amplitude of  $H_\omega \approx 100$  A/m was used for the shown time evolutions.

this as neighboring  $180^\circ$ -walls emitting waves with the same wavelength, which create standing wave characteristics inside the domains. For better clarity, reference lines along the wavefronts are drawn in Fig. 4. In the case of  $\omega/2\pi = 0.7$  GHz the reference line remains on the node indicating standing wave characteristics. At  $\omega/2\pi = 1.3$  GHz and  $\omega/2\pi = 1.9$  GHz the elastic magnetisation waves exhibit propagating wave characteristics. In the obtained overall set of data, there appears to be no systematic correlation of gradual propagation or standing wave behaviour. Since the same unaltered domain and domain wall structure exhibits, both propagating and standing waves in Fig. 4, an influence of the domain wall substructure is excluded. It should be noted that the magnetisation configuration cannot inhibit elastic waves from traveling across the magnetic boundaries formed by the magnetic domain walls. Therefore, an influence of elastic waves propagating from other domains into the domain shown here cannot be excluded.

**Magnetostatic surface spin wave emission.** Beforehand, we showed that the elastic waves follow the domain wall orientation and not the orientation of magnetisation. Now, we compare our results to regular magnetostatic surface spin waves in the Damon-Eshbach-configuration (magnon wavevector  $\mathbf{k}$  and effective field  $\mathbf{H}_{\text{eff}}$  both in-plane and  $\mathbf{H}_{\text{eff}} \perp \mathbf{k}$ ). Two different states of magnetisation are compared in Fig. 5. Figure 5(a) displays a remanent WDS domain configuration (as in Figs 1(b) and 4). The exemplary images from the temporal response at  $\omega/2\pi = 9$  GHz show the corresponding dynamic response. A line indicates the orientation of the standing spin wave nodes. Figure 5(b) shows a qualitative repetition of the experiment in Fig. 3(a) (CDS), but for magnetostatic surface spin waves obtained at the excitation frequency of  $\omega/2\pi = 9$  GHz. It is directly evident that the detected spin waves, and unlike to the elastic waves, now follow the orientation of magnetisation. The magnetostatic spin waves generated at increased frequency are not tied to the domain wall orientation but to the alignment of magnetisation (see Fig. 5). In contrast, the directionality of the elastic wave emission depends on the existence and orientation of the magnetic domain wall (compare Figs 3 and 5).

**Modelling of magnetisation wave emission.** Micromagnetic simulations<sup>31</sup> were used to clarify the origin of occurring magnetisation waves. Selected simulation results are depicted in Fig. 6. Figure 6(a,b) show the two dimensional static domain and domain wall configuration, where Fig. 6(a) displays the simulated full cross-section as  $m_x$  and Fig. 6(b) the close circumference of one  $180^\circ$  asymmetric Bloch wall as  $m_y$ . Figure 6(c) shows the differential magnetisation response along the  $y$ -direction at an excitation frequency of  $\omega/2\pi = 9$  GHz. Standing magnetostatic surface spin waves are visible inside the domains. The waves are in phase on both surfaces. Apart from the standing magnetostatic surface spin waves in the simulations, the domain walls emit low wavelength ( $\lambda < 300$  nm) propagating spin waves. Examples are depicted in Fig. 6(d,e) for a frequency of  $\omega/2\pi = 9$  GHz and  $\omega/2\pi = 10$  GHz, respectively. As the wavelengths of these spin waves are below the optical limit of detection, they do not have an experimental counterpart in this work. At frequencies below  $\omega/2\pi = 5$  GHz the low wavelength spin waves are found to be oscillating at higher harmonics of the excitation frequency. At frequencies exceeding  $\omega/2\pi = 5$  GHz this first low wavelength mode is excited directly at the excitation frequency. In addition, a second low wavelength mode is emitted at frequencies equal or higher than  $\omega/2\pi = 10$  GHz, as evident by comparison of Fig. 6(d,e). The data presented in Fig. 6(c to e) was simulated in dynamic equilibrium.

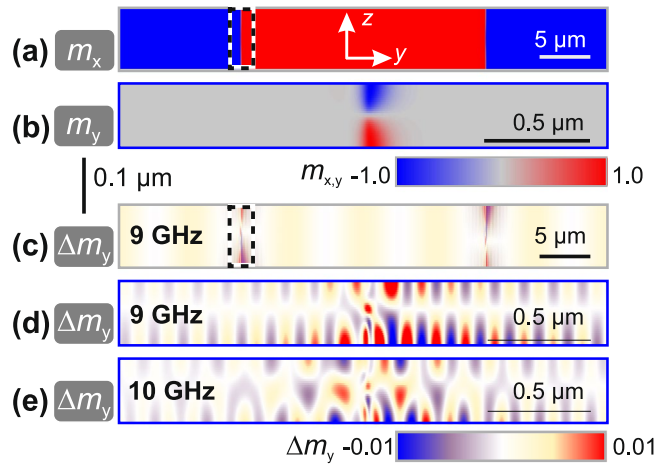


**Figure 6.** Static and dynamic micromagnetic simulation of a periodic pattern consisting of two  $180^\circ$  asymmetric Bloch walls separated by  $25\ \mu\text{m}$  wide domains. (a) Static cross-section in  $m_x$  and (b) static cross-section in  $m_y$ , from the direct circumference of the left domain wall (as indicated in (a)). (c) Differential dynamic response along  $\Delta m_y$ , at  $\omega/2\pi = 9\ \text{GHz}$ , and local differential dynamic response  $\Delta m_y$  at (d)  $\omega/2\pi = 9\ \text{GHz}$  (see also Supplementary Video 3) and (e) at  $\omega/2\pi = 10\ \text{GHz}$ .

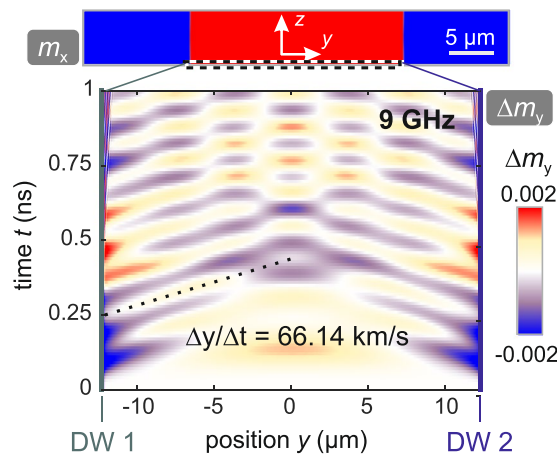


**Figure 7.** Dynamic micromagnetic simulation of the transient effect in the top layer ( $z = 120\ \text{nm}$ ) and central domain (red in Fig. 6(a)) at an excitation frequency of  $\omega/2\pi = 9\ \text{GHz}$ . The position of the two domain walls (DW 1 and DW 2) is indicated at the left and right axes. The phase velocity of the magnetostatic surface spin wave can be determined by following the wave profile along the propagation direction.

In order to determine the location, where the magnetostatic surface spin waves originate, we simulated the transient effect. The corresponding data for an excitation frequency of  $\omega/2\pi = 9\ \text{GHz}$  (compare to Fig. 6(c)) is presented in Fig. 7. Here, the evolution of dynamic magnetisation response  $\Delta m_y$  is shown for the bottom layer normal to the  $z$ -axis and in the central domain of the simulated pattern (compare to Fig. 6(a)). At  $t = 0\ \text{ns}$  the application of the sinusoidal microwave field was started. No wavefronts appear in the domain at the beginning. With increasing time, wavefronts from the domain walls propagate into the central domain and start to form superposition patterns. By following the phase of one wavefront, the phase velocity can be obtained to be  $v_{9\text{GHz}} = \Delta y/\Delta t = 66.14\ \text{km/s}$ . Our calculations prove that the spin waves originate from domain walls emitting spin waves with the same wavelength. The underlying mechanism of spin wave emission from domain walls can be understood by means of local effective fields present in the domain wall<sup>32</sup>.

Figure 8 displays the results obtained by micromagnetic simulation at a low excitation frequency of  $\omega/2\pi = 2\ \text{GHz}$  in dynamic equilibrium. The integral magnetisation along the  $y$ -axis and the external magnetic field are shown as a function of time in Fig. 8(a). A large phase shift between excitation and magnetisation is exhibited, since the excitation frequency is above the resonance frequency of the central domains in the simulation. The close circumference of the domain wall is shown in Fig. 8(b). The precession of the two domains around the domain wall can be seen directly by the change of magnetization  $\Delta m_y$ , of the domains with time. Low wavelength spin waves are visible in close proximity to the domain wall, oscillating at higher harmonics of the excitation frequency. The presumed elastic magnetisation wave branch is not reproduced by the micromagnetic calculations. As the micromagnetic modelling does not include magnetoelastic effects, this provides further

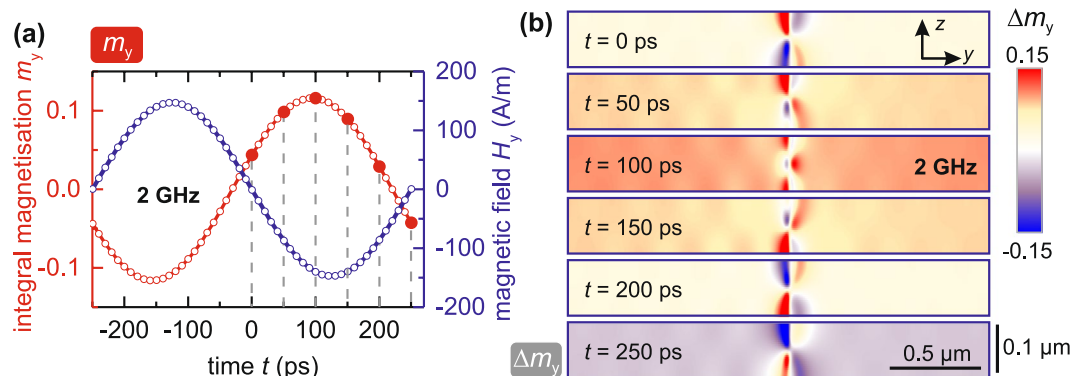


**Figure 8.** Dynamic micromagnetic simulation of the time evolution of Fig. 6(b) at  $\omega/2\pi = 2$  GHz. **(a)** Integral magnetisation and external field as a function of time. The zero-point corresponds to  $t = 5.25$  ns of applied sinusoidal field in the simulation. **(b)** Half a period of differential magnetisation  $\Delta m_y$  around the domain wall at selected time steps (red filled circles in (a)).

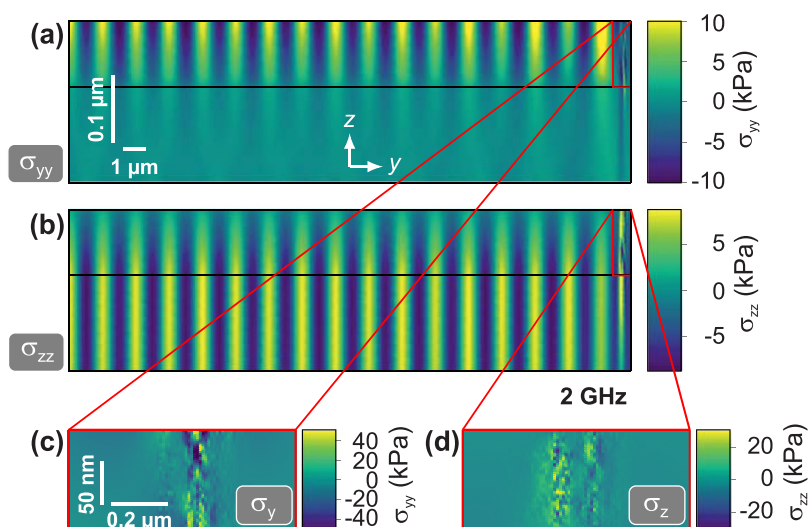


**Figure 9.** Mechanical simulation of elastic wave emission originating in the domain wall region with an excitation frequency of 2 GHz (compare to magnetisation response in Fig. 8). **(a)** Elastic stress along the  $y$ -direction  $\sigma_{yy}$  as a function of  $y$ - and  $z$ -coordinate. **(b)** Elastic stress along the  $z$ -direction  $\sigma_{zz}$  as a function of  $y$ - and  $z$ -coordinate. The horizontal black lines indicate the interface between the ferromagnet and the substrate. **(c)** Magnification of **(a)** in proximity to the excited domain wall. **(d)** Magnification of **(b)** in proximity of the excited domain wall.

evidence for the concluded alternative mechanism of magnetisation wave generation. The data clearly shows high dynamic magnetic activity  $\Delta m_y$  experienced at the domain walls. The dynamic tensioning inside the domain wall, via magnetoelastic coupling, generates elastic waves. As a result, the wavering domain wall acts as a localized alternating body force inside the (magneto)elastic material from which elastic waves penetrate the material. In the region of the domain wall the magnetisation rotates by  $\pi$ , meaning that there is at least one point in this region where the lateral magnetostriction curve has the highest possible slope. At these points the highest dependence of the dynamic strain on the varying magnetisation is expected. Magnetoelastic coupling leads to a coherent dependence of the elastic response on the dynamic magnetisation response in the domain wall.

The experimentally obtained product of wavelength and frequency leads to the assumption that the oscillating domain wall generates either a shear wave or a combination of shear and longitudinal wave. In the following we evaluate the analytical shear wave velocity and the numerical results from finite element analysis with the input from the micromagnetic modelling. Based on the calculated magnetisation response at 2 GHz (Fig. 8), the resulting local magnetostrictive strain is obtained and this local strain is transformed into an external force density acting in the elastic material. By using finite element method (FEM), this force density can be used as an input parameter for solely mechanical simulations. Figure 9 displays exemplary results of an FEM simulation at an excitation frequency of 2 GHz. Figure 9(a) shows the obtained stress along the  $y$ -direction. Clear wavefronts can be seen in the magnetic layer. In the substrate the wave amplitude decays rapidly, indicating a surface wave. In

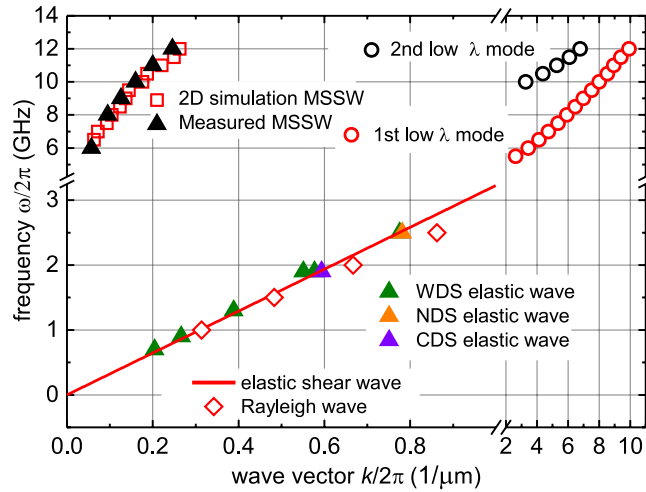


**Figure 10.** Wave vector to excitation frequency dependence of emerging wave fronts parallel to the  $x$ -axis for elastic waves and magnetostatic surface spin wave (MSSW) modes together with numerical data on the magnetostatic surface spin waves, the linear dispersion of an elastic shear wave in  $\text{Co}_{40}\text{Fe}_{60}\text{B}_{20}$ , and the calculated dispersion behavior of the Rayleigh wave. Also shown are two low wavelength modes, originating at the domain walls in the micromagnetic simulations (see Fig. 6).

contrast, Fig. 9(b) shows the stress along the  $z$ -direction. The shown wave pattern is undisturbed in the substrate, but decays in the magnetic layer with positive  $z$ -direction. This can be attributed to the free deformation exhibited at the surface of the magnetic film, leading to a reduction in stress along the out-of-plane direction. The excited surface wave profile corresponds to a Rayleigh wave. The resulting stress along  $y$ - and  $z$ -axis is consistent with the experiment, showing the magnetisation wave response only along these axes. From the stress along the  $y$  and  $z$ -axis in close circumference to the domain wall (Fig. 9(c,d)), it is directly visible that the elastic material reacts on the external stimulus given by the excited domain wall. This proves the mechanism of elastic tensioning in the domain wall region to be dominant for the generation of coherent elastic waves in the GHz-regime.

**Dispersion of distinct mode emission.** By analysing the MOKE images inside a central domain by averaging along the wavefront and subsequent fast Fourier transformation in time and space, the characteristic dependencies between excitation frequency  $\omega$  and wave vector  $k$  of the emitted spin waves are extracted. The results are directly compared to simulation results. A complete analysis of the magnetisation wave dispersion from dynamic imaging and micromagnetic simulation is displayed in Fig. 10.

The experimentally found magnetostatic spin wave dispersion is reproduced by the micromagnetic simulations. In addition, a characteristic dispersion of magnetostatic surface spin waves at low wave vector  $k$  is found at frequencies ranging from  $\omega/2\pi = 6$  GHz to  $\omega/2\pi = 12$  GHz. In the same frequency range, in the vicinity of the DWs two additional low wavelength modes are found in the simulations exhibiting a characteristic parabolic dispersion and different node number along the  $z$ -axis (one node for first low wavelength mode and two nodes for the second low wavelength mode for  $k/(2\pi) \approx 5 \mu\text{m}^{-1}$ ). When looking at the simulated integral susceptibility spectrum, no peaks are visible for these modes. No experimental evidence for such spin waves is found as the smaller wavelength spin wave modes are not accessible by MOKE imaging due to the limited spatial resolution of the optical experiment. The regime of elastic (spin) wave generation is not confirmed by the purely micromagnetic modelling.

Experimentally, the elastic magnetisation wave branch is not affected by small changes of the domain configuration. Elastic waves are observed for frequencies ranging from  $\omega/2\pi = 0.55$  GHz up to  $\omega/2\pi = 2.5$  GHz, the upper bound limited by the spatial optical resolution. The extracted  $\omega$ - $k$  dependence reveals that WDS, NDS, and CDS share a single linear dispersion relation. The dispersion is independent of the state of magnetisation. In an analytical approach, the dispersion relation is compared to the expected linear dependence for an elastic shear wave. For this the velocity of sound  $c$  was calculated using

$$c = \sqrt{\frac{G_{\text{CoFeB}}}{\rho_{\text{CoFeB}}}}, \quad (1)$$

where  $G_{\text{CoFeB}} = 70$  GPa is the shear modulus of  $\text{CoFeB}$ <sup>33</sup>. With the volumetric mass density<sup>33</sup>  $\rho_{\text{CoFeB}} = 7050 \text{ kg/m}^3$ , a shear wave propagation velocity of  $c = 3.151 \text{ km/s}$  is calculated. The corresponding dispersion relation is added to Fig. 10. It perfectly coincides with the dispersion of the experimentally found elastic wave modes. No adjustment of parameters was performed. The domain wall tied dispersion relation derived from the dynamic MOKE images corresponds to a sound velocity of  $c = 3.159 \text{ km/s}$ .

Furthermore, mechanical finite element calculations were conducted for four excitation frequencies from 1 GHz to 2.5 GHz using the micromagnetically obtained magnetisations to calculate the local force densities.

Both, the elastic shear wave and the extracted Rayleigh wave, display good agreement with the measured wave dispersion. This confirms the presumed elastic wave mechanism. Moreover, the dispersion relation of the elastic waves provides proof for the domain wall mediated generation of elastic waves.

## Conclusions

Distinct modes of magnetisation waves are generated from domain wall dynamics. The existence of the waves is confirmed by direct time resolved magneto-optical imaging. Standing magnetostatic surface spin waves in the Damon-Eshbach configuration and elastic magnetisation waves are excited by magnetic domain walls acting as antennas. The experimental investigation shows that the magnetostatic surface spin waves follow the alignment of magnetisation orientation in the domains. In contrast, the elastic waves are independent of the alignment of the excitation field and the state of magnetisation inside the domains. The orientation of the elastic waves is purely bound to the orientation of the domain walls. They are solely and directly connected to the dynamically excited domain walls. The direction of elastic wave propagation can be tuned with the orientation of the domain walls.

Together with the experimental evidence, our analysis of the linear dispersion relation clearly shows that the origin of the elastic mode stems from coherent elastic waves generated at the domain walls in the magnetostrictive thin films through magnetoelastic coupling. Origin is a dynamic tensioning inside the excited domain walls of the magnetostrictive material as confirmed by finite element simulations.

The discovery of the alternative mode of acoustic wave generation from domain walls could help building broadband and reconfigurable sources of low damped magnetoelastic spin waves for future applications without the need for piezoelectric substrates or elements. The magnetostatic and elastic magnetisation waves emitted by high angle domain walls show that magnetic domain walls can be used as reconfigurable sources for coherent emission of magnetisation waves up to high frequencies into the GHz-regime.

## Methods

**Magnetostrictive CoFeB thin film stripe arrays.** A  $Ta(5\text{ nm})/Co_{40}Fe_{40}B_{20}(120\text{ nm})/Ru(3\text{ nm})$  layer was prepared by sputter deposition on a glass  $SiO_2$  wafer with a thickness  $t = 800\ \mu\text{m}$ . The Ru covering layer forms a protective layer over the ferromagnetic structures to avoid oxidation and corrosion. Saturation polarisation of the ferromagnetic material is  $J_s = 1.5T$ . An induced uniaxial magnetic anisotropy of  $K_u = 1300\text{ J/m}^3$  is introduced by applying a magnetic field of  $H_{dep} = 8\text{ kA/m}$  during magnetic layer deposition<sup>30</sup>. The saturation magnetostriction is  $\lambda_s \approx 25 \times 10^{-6}$ <sup>34</sup>. To ensure the generation of periodic domain walls the film is patterned into elongated stripes with the dimension of  $40\ \mu\text{m} \times 10\text{ nm}$  via standard photolithography and selective ion beam etching. Substrate pieces of  $10\text{ mm} \times 10\text{ mm}$  were cut by wafer sawing from the full wafer.

**Dynamic magnetisation characterisation.** The dynamic magnetic characteristics, e.g. magnetic permeability spectra, were obtained by pulsed inductive microwave magnetometry (PIMM)<sup>35</sup> with an in-plane magnetic field pulse of  $H_{pulse} \approx 3.0\text{ A/m}$  and a rise time of  $t_{rt,10-90} \leq 50\text{ ps}$  (see Supplementary Fig. 1). The measurements were performed with varying bias field  $H_{ext}$ . The time domain data was transferred into the frequency domain by fast Fourier transformation, from which the dynamic magnetic permeability spectra were obtained. From the experiments the individual domain resonance in the stripes and the effective damping parameter  $\alpha = 0.008$  of the material were obtained.

**Component selective time resolved magneto-optical wide-field imaging.** To experimentally probe wave emission, we apply time-resolved magneto-optical wide field imaging<sup>27</sup> based on the magneto-optical Kerr effect (MOKE) to a ferromagnetic thin film structure. For all magneto-optical images a specialized magneto-optical wide-field microscope is used that allows not only for static domain imaging, but also for time-resolved observations by using a pulsed Nd:YVO<sub>4</sub> laser illumination system with 7 ps pulse width and a repetition rate of 50 MHz for stroboscopic imaging. The laser wavelength is  $\lambda = 532\text{ nm}$  and the numerical aperture of the used long-distance objective lens is  $NA = 0.6$ . This transfers to a spatial resolution of about 450 nm.

A motorised stage is implemented in the setup allowing for precise and reproducible positioning of a lens, resulting in automatic control of the angle of incidence and magneto-optical sensitivity. A coplanar waveguide is utilised to generate a homogeneous high frequency magnetic field  $H_{wg}$ . The central wave guide consists of a  $160\ \mu\text{m}$  wide and  $17.5\ \mu\text{m}$  thick centre conductor. The sample is positioned with the magnetic surface down on top of the waveguide and the sample direction relative to the dynamic magnetic field can be freely adjusted. To influence the domain pattern, and thus the domain wall determined magnetisation dynamics, the magnetic field history is varied in angle and strength.

The dynamic change of individual magnetisation components is probed by a component selective imaging process<sup>28</sup>. It allows for direct measurement of in-plane and out-of-plane magnetisation components by dynamic MOKE microscopy. In order to measure only dynamic magnetisation contrast each dynamic MOKE image at a phase  $\phi$  is subtracted by an image of phase  $\phi - \pi$ . The measurement process involves the measurement using two non-zero angles of incidence differing by a sign change and subtraction of those two magneto-optical sensitivities. By following this procedure the polar magneto-optical contrast cancels out, leading to pure magnetic in-plane response. By this also a possible birefringence or photo-elastic effect resulting from the magnetoelastic interaction cancels for the detection of the pure in-plane magnetisation components, as the reflection coefficients are symmetric for two opposing angles of incidence<sup>36</sup>. Only magnetic contrast changes are visible in the quantitative dynamic in-plane images ( $\Delta m_x, \Delta m_y$ ).

**Micromagnetic modelling.** Two-dimensional micromagnetic simulations using mumax<sup>3</sup><sup>31</sup> were used to explain the experimental results. In accordance with the experiments, in the numerical simulations a two-dimensional two domain state of domain width  $w = 25\ \mu\text{m}$  was simulated in the  $y,z$  cross-section plane. Periodic boundary conditions along  $x$ - and  $y$ -directions were applied. A grid size of  $1 \times 12500 \times 30$  with a cell

size of  $4 \times 4 \times 4 \text{ nm}^3$  was used. Calculations were performed with an exchange constant  $A = 15 \text{ pJ/m}^3$ , a damping constant  $\alpha = 0.008$ , an uniaxial anisotropy  $K_u = 1300 \text{ J/m}^3$ , a saturation magnetisation of  $M_s = 1200 \text{ kA/m}$  and at a temperature of  $T = 0 \text{ K}$ . The domain wall was excited with a magnetic field amplitude of  $H_{\text{ex}} = 145 \text{ A/m}$ . The homogeneous high frequency field was applied at frequencies ranging from  $\omega/2\pi = 0.5 \text{ GHz}$  to  $\omega/2\pi = 12 \text{ GHz}$ . In order to gain comparable results and gain purely dynamic magnetisation response  $\Delta m_y$ , each simulated time frame at excitation phase  $\phi$  is subtracted by the corresponding time frame at excitation phase  $\phi - \pi$ .

**Mechanical finite element modelling.** The components of the magnetostrictive strain tensor  $\underline{\varepsilon}^{\text{mag}}$  are given by<sup>26</sup>

$$\varepsilon_{ik}^{\text{mag}} = \frac{3}{2} \lambda_s \left( m_i m_k - \frac{1}{3} \delta_{ik} \right), \quad (2)$$

where  $\lambda_s = 25 \cdot 10^{-6}$  is the saturation magnetostriction,  $m_{ik}$  are the components of the magnetisation vector and  $\delta_{ik}$  is the Kronecker delta. In order to calculate the elastic response of the material on the domain wall excitation, we calculated the force density  $\mathbf{f}$  caused by magnetostriction<sup>38</sup>:

$$\mathbf{f} = \nabla \cdot \underline{\underline{c}} \cdot \underline{\varepsilon}^{\text{mag}}. \quad (3)$$

Here,  $\underline{\underline{c}}$  denotes the stiffness tensor. By using the two-dimensional data set of magnetisation response obtained from micromagnetic simulations, we calculated the local force density distribution in the circumference of the domain wall due to magnetostriction. Then a fast Fourier transformation is applied in the time domain. For each local data point the complex force density on the excitation frequency is selected. This local complex force density is then used as an input parameter for a mechanical COMSOL Multiphysics<sup>®39</sup> calculation.

The COMSOL Multiphysics<sup>®</sup> model consists of a  $116 \text{ nm}$  thick layer of a magnetostrictive amorphous ferromagnetic  $\text{Co}_{40}\text{Fe}_{40}\text{B}_{20}$  with a length of  $50 \mu\text{m}$ . To reduce the computation time, the substrate was assumed to be infinitely thick, hence after  $10 \mu\text{m}$  of the substrate low reflecting boundary conditions are applied. These conditions are as well applied for the left and right boundary of the simulation area to avoid standing waves due to reflection. The excitation area around the domain wall is placed in the middle of the magnetostrictive layer with a size of  $808 \times 116 \text{ nm}^2$  with a cell size of  $4 \times 4 \text{ nm}^2$ , where the calculated forces are applied as a boundary load. Due to the numerical gradient evaluation, the force input was reduced by one cell along the  $z$ -direction compared to the micromagnetically simulated magnetisation distribution. For the calculation the following isotropic material parameters were used a Young's modulus of  $E_{\text{CoFeB}} = 182 \text{ GPa}$ , a Poisson's ratio of  $\nu_{\text{CoFeB}} = 0.3$ , and a density of  $\rho_{\text{CoFeB}} = 7050 \text{ kg/m}^3$ <sup>33</sup>, and respectively  $E_{\text{glass}} = 82 \text{ GPa}$ ,  $\nu_{\text{glass}} = 0.206$ , and  $\rho_{\text{glass}} = 2510 \text{ kg/m}^3$ <sup>40</sup>.

The datasets generated during and/or analysed during the current study are available from the corresponding author on reasonable request.

## References

- Chumak, A. V., Vasyuchka, V. I., Serga, A. A. & Hillebrands, B. Magnon spintronics. *Nat. Phys.* **11**, 453–461 (2015).
- Kruglyak, V., Demokritov, S. & Grundler, D. Magnonics. *J. Phys. D: Appl. Phys.* **43**, 264001 (2010).
- Lenk, B., Ulrichs, H., Garbs, F. & Münzenberg, M. The building blocks of magnonics. *Phys. Reports* **507**, 107–136 (2011).
- Mushenok, F. B. *et al.* Broadband conversion of microwaves into propagating spin waves in patterned magnetic structures. *Appl. Phys. Lett.* **111**, 042404 (2017).
- Lohman, M., Mozooni, B. & McCord, J. Homogeneous microwave field emitted propagating spin waves: Direct imaging and modeling. *J. Magn. Magn. Mater.* **450**, 7–12 (2018).
- Whitehead, N. J., Horsley, S. A. R., Philbin, T. G., Kuchko, A. N. & Kruglyak, V. V. Theory of linear spin wave emission from a Bloch domain wall. *Phys. Rev. B* **96**, 064415 (2017).
- Winter, J. M. Bloch wall excitation. application to nuclear resonance in a Bloch wall. *Phys. Rev.* **124**, 452–459 (1961).
- Shimokhin, I. A. On the Gilinskii branch of the spectrum of excitations of a domain wall in uniaxial ferromagnetics. *physica status solidi (b)* **167**, 243–250 (1991).
- Alekseev, A. M., Dötsch, H., Kulagin, N. E., Popkov, A. F. & Synogach, V. T. Microwave excitations of a domain wall in a cubic magnet with induced anisotropy. *Tech. Phys.* **44**, 657–663 (1999).
- Trützschler, J., Sentosun, K., Mozooni, B., Mattheis, R. & McCord, J. Magnetic domain wall gratings for magnetization reversal tuning and confined dynamic mode localization. *Sci. Reports* **6**, 30761 (2016).
- Wagner, K. *et al.* Magnetic domain walls as reconfigurable spin-wave nanochannels. *Nat. Nanotechnol.* **11**, 432–436 (2016).
- Pirro, P. *et al.* Experimental observation of the interaction of propagating spin waves with Néel domain walls in a Landau domain structure. *Appl. Phys. Lett.* **106**, 232405 (2015).
- Wintz, S. *et al.* Magnetic vortex cores as tunable spin-wave emitters. *Nat. Nanotechnol.* **11**, 948–953 (2016).
- Roy, P. E., Trypiniotis, T. & Barnes, C. H. W. Micromagnetic simulations of spin-wave normal modes and the resonant field-driven magnetization dynamics of a  $360 \text{ nm}$  domain wall in a soft magnetic stripe. *Phys. Rev. B* **82**, 134411 (2010).
- Van de Wiele, B., Hämmäläinen, S. J., Baláz, P., Montoncello, F. & van Dijken, S. Tunable short-wavelength spin wave excitation from pinned magnetic domain walls. *Sci. Reports* **6**, 21330 (2016).
- Mozooni, B. & McCord, J. Direct observation of closure domain wall mediated spin waves. *Appl. Phys. Lett.* **107**, 042402 (2015).
- Yuan, S. W. & Bertram, H. N. Magnetic thin film domain wall motion under dynamic fields. *J. Appl. Phys.* **72**, 1033–1038 (1992).
- Mozooni, B., von Hofe, T. & McCord, J. Picosecond wide-field magneto-optical imaging of magnetization dynamics of amorphous film elements. *Phys. Rev. B* **90**, 054410 (2014).
- Mullenix, J., El-Ghazaly, A., Lee, D. W., Wang, S. X. & White, R. M. Spin-wave resonances in the presence of a Bloch wall. *Phys. Rev. B* **89**, 224406 (2014).
- Barra, A., Mal, A., Carman, G. & Sepulveda, A. Voltage induced mechanical/spin wave propagation over long distances. *Appl. Phys. Lett.* **110**, 072401 (2017).
- In literature the exhibited waves are often discussed in terms of magnetoelastic spin waves. To distinguish between traditional spin waves and the elastically excited spin waves we refer to them as elastic or elastic magnetization waves. Acoustic waves would also be a possible term.

22. Cherepov, S. *et al.* Electric-field-induced spin wave generation using multiferroic magnetoelectric cells. *Appl. Phys. Lett.* **104**, 082403 (2014).
23. Lord, A. E. Elastic wave radiation from simply-vibrating 180° magnetic domain walls. *Acta Acustica united with Acustica* **18**, 187–192 (1967).
24. Foerster, M. *et al.* Direct imaging of delayed magneto-dynamic modes induced by surface acoustic waves. *Nat. Commun.* **8**, 407 (2017).
25. Weiler, M. *et al.* Elastically driven ferromagnetic resonance in nickel thin films. *Phys. Rev. Lett.* **106**, 117601 (2011).
26. Hubert, A. & Schäfer, R. *Magnetic domains: the analysis of magnetic microstructures* (Springer Science & Business Media, 2008).
27. McCord, J. Progress in magnetic domain observation by advanced magneto-optical microscopy. *J. Phys. D: Appl. Phys.* **48**, 333001 (2015).
28. Holländer, R. B., Müller, C., Lohmann, M., Mozooni, B. & McCord, J. Component selection in time-resolved magneto-optical wide-field imaging for the investigation of magnetic microstructures. *J. Magn. Magn. Mater.* **432**, 283–290 (2017).
29. Queitsch, U. *et al.* Domain wall induced modes of high-frequency response in ferromagnetic elements. *J. Appl. Phys.* **100**, 093911 (2006).
30. Hengst, C., Wolf, M., Schäfer, R., Schultz, L. & McCord, J. Acoustic-domain resonance mode in magnetic closure-domain structures: A probe for domain-shape characteristics and domain-wall transformations. *Phys. Rev. B* **89**, 214412 (2014).
31. Vansteenkiste, A. *et al.* The design and verification of mumax3. *AIP Adv.* **4**, 107133 (2014).
32. Schlömann, E. Generation of spin waves in nonuniform magnetic fields. i. conversion of electromagnetic power into spin-wave power and vice versa. *J. Appl. Phys.* **35**, 159–166 (1964).
33. Graczyk, P. & Krawczyk, M. Coupled-mode theory for the interaction between acoustic waves and spin waves in magnonic-phononic crystals: Propagating magnetoelastic waves. *Phys. Rev. B* **96**, 024407 (2017).
34. O'Handley, R. C. *Modern Magnetic Materials: Principles and Applications* (John Wiley & Sons, Inc., 2000).
35. Silva, T. J., Lee, C. S., Crawford, T. M. & Rogers, C. T. Inductive measurement of ultrafast magnetization dynamics in thin-film permalloy. *J. Appl. Phys.* **85**, 7849–7862 (1999).
36. Silverman, M. P. & Badoz, J. Light reflection from a naturally optically active birefringent medium. *J. Opt. Soc. Am. A* **7**, 1163–1173 (1990).
37. Conca, A. *et al.* Low spin-wave damping in amorphous Co<sub>40</sub>Fe<sub>40</sub>B<sub>20</sub> thin films. *J. Appl. Phys.* **113**, 213909 (2013).
38. Liang, C.-Y. *et al.* Modeling of magnetoelastic nanostructures with a fully coupled mechanical-micromagnetic model. *Nanotechnol.* **25**, 435701 (2014).
39. COMSOL Multiphysics® v. 5.2. [www.comsol.com](http://www.comsol.com). COMSOL AB, Stockholm, Sweden.
40. Crystran. N-BK7 glass. <https://www.crystran.co.uk/optical-materials/optical-glass-n-bk7-and-others> (2018).

## Acknowledgements

Funding through the German Research Council (DFG, MC9/10-2) is highly appreciated. J.M. thanks the DFG for support through their *Heisenberg Programme* (DFG, MC9/9-1, MC9/9-2). J.S. and M.G. thank the DFG for support through the Collaborative Research Centre CRC 1261 *Magnetoelectric Sensors: From Composite Materials to Biomagnetic Diagnostics*. We thank Roland Mattheis for thin film preparation and Ingolf Mönch for help with the sample preparation. We further thank Mathis Lohman for assistance with the initial imaging experiments.

## Author Contributions

J.M. proposed and supervised the study. R.B.H. and C.M. performed the imaging experiments. R.B.H. conducted the micromagnetic simulations. J.S. and M.G. devised the FEM simulations. J.S. carried out the simulations. J.M. and R.B.H. wrote the main manuscript with assistance from C.M. and J.S. R.B.H. wrote the supplementary information. All authors interpreted the data, discussed the results, reviewed, and commented on the manuscript.

## Additional Information

**Supplementary information** accompanies this paper at <https://doi.org/10.1038/s41598-018-31689-8>.

**Competing Interests:** The authors declare no competing interests.

**Publisher's note:** Springer Nature remains neutral with regard to jurisdictional claims in published maps and institutional affiliations.



**Open Access** This article is licensed under a Creative Commons Attribution 4.0 International License, which permits use, sharing, adaptation, distribution and reproduction in any medium or format, as long as you give appropriate credit to the original author(s) and the source, provide a link to the Creative Commons license, and indicate if changes were made. The images or other third party material in this article are included in the article's Creative Commons license, unless indicated otherwise in a credit line to the material. If material is not included in the article's Creative Commons license and your intended use is not permitted by statutory regulation or exceeds the permitted use, you will need to obtain permission directly from the copyright holder. To view a copy of this license, visit <http://creativecommons.org/licenses/by/4.0/>.

© The Author(s) 2018